Journal of Fluids and Structures 145 (2026) 104566

Contents lists available at ScienceDirect

Journal of Fluids and Structures

journal homepage: www.elsevier.com/locate/jfs

Wave-induced boundary layers underneath a flexible structure

Esra Uksul [a,*], Angeliki Laskari [a], Sebastian Schreier [b], Christian Poelma [a]

[a] Multiphase Systems, Department of Process and Energy, Delft University of Technology, Delft, The Netherlands
[b] Ship Hydromechanics, Department of Maritime and Transport Technology, Delft University of Technology, Delft, The Netherlands

ARTICLE INFO

Keywords:
Wave boundary layer
Flexible floating structures
Wave structure interactions
VLFS
Stokes boundary layer model
Surface waves

ABSTRACT

The interaction between propagating waves and flexible floating structures remains poorly understood, particularly in terms of interface boundary layer characteristics, which play a role in influencing wave attenuation and energy dissipation. In this study, phase-locked Particle Image Velocimetry was used to capture velocity fields beneath a continuous, compliant structure subjected to regular waves of varying order and steepness. The results confirm the formation of a distinct wave-induced boundary layer at the fluid-structure interface. For second-order waves with low steepness ($H/\lambda = 0.02$), an adapted form of Stokes' second problem predicts the boundary layer thickness, velocity overshoot, and exponential decay with depth reasonably well. However, for steeper second-order or third-order waves ($H/\lambda = 0.033$–0.064), the experimental data reveal significant deviations from the model - specifically in the boundary layer structure and in the slope of the velocity profile for attenuating waves. These discrepancies suggest that classical linear theory is insufficient in capturing the full complexity of wave-structure interactions as wave steepness increases and nonlinear effects become more pronounced.

1. Introduction

Boundary layers formed by oscillatory wave motion are central to understanding energy dissipation, momentum transfer, and mixing processes in aquatic environments. Traditionally, research in this field focused on bottom boundary layers (BBLs), where the interaction of wave-induced flows with the seabed played a critical role in sediment transport, turbulence generation, and large-scale basin dynamics (Munk, 1966; Imberger, 1998). The structure and scaling of these BBLs, particularly under oscillatory forcing, are well described by theoretical frameworks such as Stokes' second problem, which predict boundary layer thickness to scale with $\sqrt{\nu T}$, where ν is the kinematic viscosity and T is the wave period (Schlichting and Kestin, 1961).

In contrast to the extensive body of work on wave-induced bottom boundary layers, less attention was given to boundary layers forming at the upper side of the fluid domain, where wave motion interacts with either natural or engineered floating surfaces. These boundary layers develop beneath overlying structures, where the interface is not rigid but deformable. While the flow retains its oscillatory nature, the presence of a compliant boundary introduces complex fluid-structure interactions that differ fundamentally from those observed near solid beds.

While such configurations occur in both natural systems (e.g., sea ice in polar regions) and maritime engineering applications (e.g., floating solar platforms), experimental studies that resolve the velocity field in this near-surface region remain scarce. In sea ice research, wave propagation through continuous and fragmented ice sheets in the transition zone between open water and sea (known as the marginal ice zone) governs key processes such as wave attenuation, scattering, and ice break-up

* Corresponding author.
E-mail address: e.uksul@tudelft.nl (E. Uksul).

https://doi.org/10.1016/j.jfluidstructs.2026.104566
Received 22 September 2025; Received in revised form 6 February 2026; Accepted 17 March 2026
Available online 6 April 2026

(Squire, 2007; Mosig et al., 2015). Likewise, for Very Large Floating Structures (VLFS), the interaction of waves with flexible, buoyant platforms present challenges for predicting hydrodynamic loads, structural response, and local flow behavior beneath the structure (Zhang and Schreier, 2022; Zhang et al., 2025).

The role of boundary layer dynamics in these interactions has been increasingly recognized (Yiew et al., 2019; Sutherland et al., 2017), with recent laboratory studies confirming the formation of a wave-induced boundary layer beneath ice floes (Rabault et al., 2019; Orzech et al., 2022). However, these studies primarily focused on discontinuous ice fields, where eddy generation from floe collisions dominate the dynamics. In contrast, the flow beneath continuous, elastic surfaces-where wave-structure interactions are governed by flexural rigidity and hydroelastic response-remain poorly characterized. While a number of theoretical and numerical studies explored viscoelastic responses of ice and flexible materials (Hermans, 2004; Wang and Tay, 2011), direct experimental validation at the fluid-structure interface is still lacking. For example, laboratory experiments by Sree et al. (2018) using viscoelastic PDMS sheets demonstrated material-dependent changes in wave propagation, but did not resolve the detailed velocity fields beneath the structure - leaving the boundary layer behaviour unquantified.

From an engineering standpoint, flexible VLFS gained attention as platforms for offshore solar photovoltaics, especially as land-based energy systems face spatial limitations. These floating structures, often composed of compliant materials, interact with wave fields in ways that were difficult to predict using classical, inviscid theories. As highlighted in our earlier work (Uksul et al., 2025), the wave-structure interaction in such cases affects both wave attenuation and subsurface velocity field, having implications for the design and longevity of such systems. Notably, our experimental results demonstrated that 2nd order Stokes wave theory predicts profiles of the horizontal velocity under a flexible structure more accurately than under a rigid one, where deviations from exponential decay and signs of a wave boundary layer (WBL) emerged (Uksul et al., 2025). This suggests that the assumption of inviscid flow in many wave-structure interaction models is insufficient, particularly for highly flexible structures.

Moreover, in both sea ice and VLFS applications, classical Stokes boundary layer theory, foundational for understanding laminar oscillating flows, may be inadequate for predicting the actual velocity structure near deformable boundaries. The limited measurements available (e.g., Rabault et al., 2019; Orzech et al., 2022; Uksul et al., 2025) highlighted the difficulty of obtaining velocity profiles near such interfaces, often due to the small boundary layer thickness and the influence of structural motion. Yet, accurate characterization of this region is crucial: as shown in sea ice studies, boundary-layer shear stresses can contribute significantly to wave energy dissipation (Weber, 1987; Sutherland et al., 2017), and wave-induced stresses can promote structural breakup under dynamic wave loading (Zhao and Shen, 2015; Herman, 2017).

To address this gap, the present study experimentally investigates velocity profiles beneath a continuous, flexible floating structure subjected to regular surface waves of varying Stokes order and wavelength. Using high-resolution Particle Image Velocimetry (PIV), we resolve the near-interface velocity field and characterize the wave-induced boundary layer. By systematically varying the wave nonlinearity-through second, and third order Stokes waves-we assess how wave order influences the velocity structure and the formation of the boundary layer under a compliant surface. The velocity profiles are analyzed to evaluate how both wave properties and structural flexibility affect the underlying flow. Experimental results are compared against classical free-surface wave theory and an adapted version of Stokes' second problem to quantify the impact of the structure on flow development. To characterize the near-boundary dynamics, the boundary layer thickness is extracted from experimental data and compared to theoretical predictions, including the classical laminar scaling from Stokes' theory. This comparative method assesses whether existing models adequately capture the physics of wave-induced flows beneath compliant structures and helps define the limits of their applicability. By systematically comparing measured velocity fields with theoretical predictions, this study contributes to the understanding of wave-structure interactions at compliant boundaries, with potential implications for environmental modeling and the design of offshore floating systems.

2. Methods

2.1. Experimental setup

The study was carried out in Towing Tank No. 2 at the Department of Maritime and Transport Technology, TU Delft. Providing a well-regulated environment for hydrodynamic studies, the facility measures 85 m in length and 2.75 m in width. During the experiments, the water depth d was maintained at 1.22 m, with a recorded temperature of 18 °C. The temperature was monitored but not actively regulated; variations remained within approximately ±0.5 °C, recorded at the same reference time for each run. The corresponding changes in water density and viscosity over this range are small and are not expected to affect the results significantly.

Wave conditions were generated using a piston/flap-type wave maker, operated in piston mode to produce the desired wave characteristics. To reduce wave reflections and maintain stable wave propagation, a damping beach was installed at the opposite end of the tank, promoting consistent and repeatable measurement conditions.

The flexible structure used in this study has a length of $L = 5$ m, width $B = 1.02$ m, and thickness $H_t = 4.8$ mm. It is made of closed-pore neoprene foam with a density of $145.42\,\mathrm{kg/m^3}$ and a Young's modulus of $E = 828$ kPa. The flexibility of the structure can be described by the characteristic length $\lambda_c = 0.193$ m (Suzuki et al., 2007; Suzuki and Yoshida, 1996) which relates bending stiffness and hydrostatic restoring forces. The structure's stiffness was measured as described by Schreier and Jacobi (2021a). The geometry and material were selected to closely match that configuration to enable direct comparison. This choice provided a thin, flexible floating sheet that can closely follow the imposed wave motion, while leaving space to the tank sidewalls.

To ensure stability under wave forcing, the structure was secured using four mooring lines. The front moorings consisted of high-stiffness Dyneema lines with a diameter of 0.2 mm, while the rear moorings used pre-stretched elastic sewing threads with a diameter

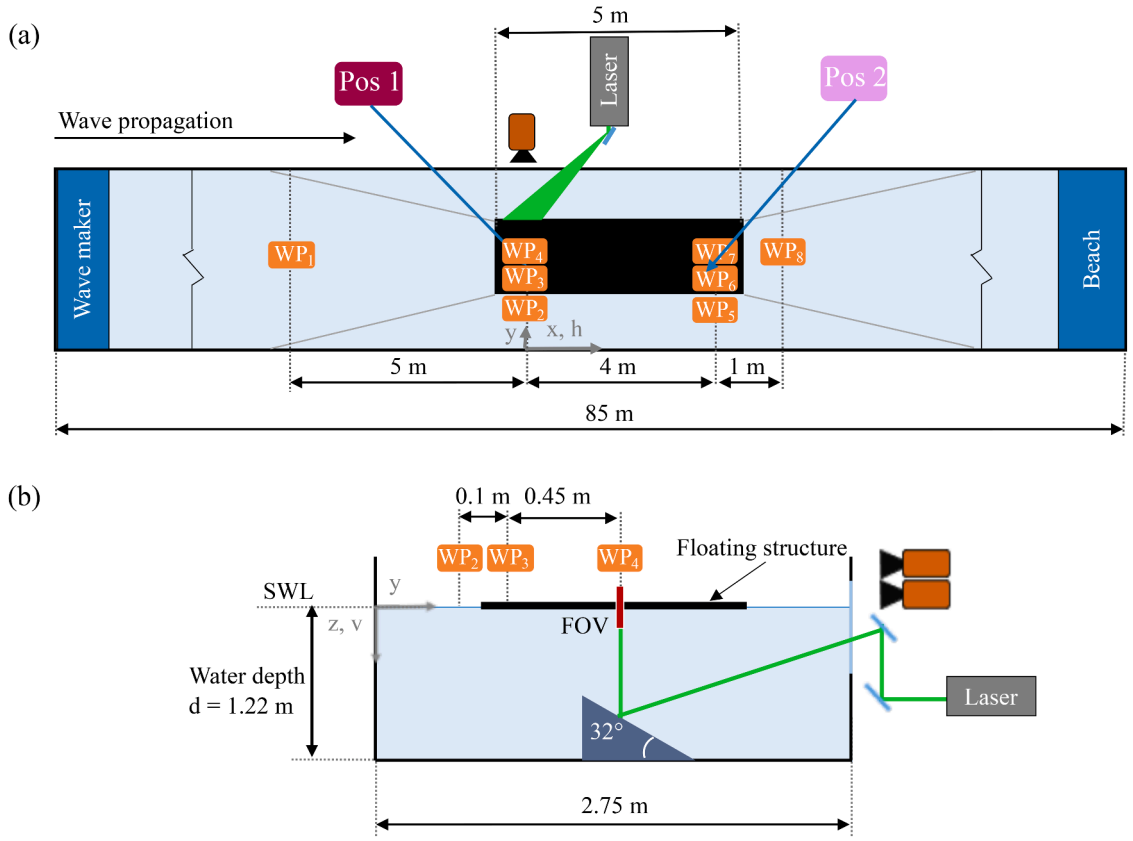

Fig. 1. Schematic of wave tank and experimental setup: top view (a) and cross section (b).

of 0.5 mm and a pretension of 0.2 N. The front mooring lines provided a stiff horizontal constraint, minimizing translation of the leading edge in the streamwise and spanwise directions. The rear elastic moorings provided a restoring force to maintain the mean position while allowing compliance of the trailing edge during wave-induced deformation. As a result, the structure was free to heave and to deform with the wave shape, while horizontal drift was minimized by the mooring arrangement.

With optical access through the tank's side window, high-resolution, planar PIV measurements were conducted to visualize the flow field underneath the floating structure. Concurrently, wave probes positioned along the tank measured real-time wave (and structure) elevations. An overview of the experimental setup is sketched in Fig. 1.

Regarding PIV, a 3 mm-thick laser sheet, generated by a double-pulse laser, illuminated the PIV measurement region. Mirrors redirected the laser sheet toward the measurement area, providing consistent illumination at the structure's midplane for flow analysis. At the tank's center plane, two PIV cameras captured a field of view (FOV) of 9 cm × 8 cm with an image resolution of 27 pixels/mm each. The cameras were placed one above the other, with their FOVs overlapping about 1 cm. A PTU controller (LaVision, Göttingen, Germany) synchronized the system components, while DaVis 10 software regulated data acquisition and image capture. A summary of the PIV system specifications and equipment is provided in Table 1.

Table 1
Summary of the PIV system parameters.

Laser	Litron Bernoulli Nd:YAG
Wavelength λ	532 nm
Output energy per laser	100 mJ per pulse
Max. frequency	50 Hz
Camera	LaVision Imager sCMOS CLHS
Resolution	2560 × 2160 pixels
Pixel pitch	6.5 µm
Lens	Nikon Macro Lens
Focal length f	200 mm
Aperture	f/4

A dedicated Arduino Micro was integrated to synchronize measurement timing with the wave phase, ensuring flow dynamics were recorded at consistent points within the wave cycle. For seeding, neutrally buoyant hollow glass spheres (10 μm diameter, Sphericel, Potters Industries) were dispersed in the water as tracers. To minimize particle clustering and promote homogeneous dispersion throughout the measurement volume, a surfactant (Tween) was added, as recommended by Westerweel (1995)

Phase-locked particle image pairs were acquired at 25 Hz for all cases. The inter-frame time Δt was adjusted per wave case and is listed in Table 2. The velocity vector fields were computed from the particle image pairs using commercial PIV analysis software (PIVTEC GmbH, Göttingen, Germany), employing a final interrogation window size of 48 × 24 pixels with 50% overlap, resulting in a resolution in terms of vector spacing of approximately 0.47 mm. Vector validation was performed using a normalized median test (threshold 5) with a minimum correlation criterion of 50%. A typical 3–6% of vectors per instantaneous field were flagged as invalid/outliers. Where available, these vectors were replaced by lower-order correlation peaks and no interpolation-based outlier replacement was used. Attempts to further increase the effective spatial resolution, particularly in the z direction near the interface, were constrained by the camera standoff distance exceeding 2 m. Further optical zoom reduced particle image density and degraded correlation quality, and higher particle concentrations were not feasible because seeding was applied manually and locally and the structure could not be removed between runs.

Wave elevation data were acquired using eight probes: four acoustic probes (WP2, WP3, WP5, WP6), two resistance-based wired probes (WP1, WP8), and two laser distance meters (WP4, WP7). These probes were strategically positioned along the tank for comprehensive wave height measurements. WP1, located at the midplane of the tank, served as both a wave probe and a camera trigger, as discussed in Uksul et al. (2025). The resistance-based wave probes were developed in-house and underwent daily calibration to maintain accuracy. Calibration was conducted in 10 mm increments over a 200 mm range, with the highest calibration errors occurring near the sensor range extremities. The maximum recorded discrepancy within the measurement range was 3.4 %. The acoustic wave probes (General Acoustics, Kiel, Germany) operated within a measurement range of 200 mm to 1200 mm, with a sampling rate of 100 Hz, an accuracy of 1 mm, and a resolution of 0.18 mm. To maintain accuracy, a reference probe continuously monitored the speed of sound in air to enable self-calibration, achieving an accuracy of 0.1 m/s. Their non-invasive design made them compatible with PIV measurements, allowing wave measurements without interfering with the flow field. Additionally, their high resolution and precision enabled detailed wave elevation measurements even in highly dynamic flow conditions.

In this study, five different wave cases were tested (see Table 3). They were selected to cover a range of wave steepnesses (H/λ) and wavelengths (λ), with H the wave height, as detailed in Section 2.2. Each wave case was repeated in at least three runs. A run consisted of a wave train, i.e., a consecutive sequence of individual wave cycles, generated with a short ramp-up, a steady-state segment, and a ramp-down. PIV acquisition was restricted to the steady-state segment, and sufficient wave cycles per run were recorded to ensure statistical convergence (see Section 2.5). The total wave train duration (per run) was adjusted according to group speed, to limit the effect of reflections from the beach, and runs were separated by a settling time to restore still-water conditions. Details of the wave conditions are provided in Table 3.

Table 2
PIV acquisition settings. Δt refers to the time between PIV image pairs.

Case	Δt [μs]	Frame rate [Hz]
W3-2	4400	25
W3-3	700	25
W5-2	3200	25
W5-3	1000	25
W6-2	6100	25

Table 3
Wave cases. The classification of wave orders follows Le Méhauté (2013).

Case	**T** [s]	λ [m]	H/λ	H [m]	Wave order
W3-2	1.4	3.02	0.02	0.06	2
W3-3	1.4	3.02	0.064	0.195	3
W5-2	1.0	1.56	0.02	0.03	2
W5-3	1.0	1.56	0.064	0.10	3
W6-2	0.65	0.66	0.033	0.022	2

2.2. Wave theory

This section introduces the wave-related notation and parameters used throughout the paper. The specific Stokes-wave formulation adopted in this study and used in the subsequent analysis is stated explicitly in Section 2.3. As surface gravity waves propagate, the associated velocity field decays hyperbolically with depth, as described by linear wave theory, here under the assumptions of intermediate water depth (where $\frac{1}{20} \leq \frac{d}{\lambda} \leq \frac{1}{2}$). Near the surface, the horizontal velocity exhibits periodic oscillations, driven by wave-induced motion (Dean, 1990). The waves analyzed in this study (see Table 3) fall within the range of both second- and third-order Stokes waves, as defined by classical Stokes wave theory (henceforth denoted with SWT), which extends linear wave theory to incorporate nonlinear effects. The velocity components can then be represented using first-, second-, and third-order Stokes wave formulations, where increasing wave order enhances the accuracy of steep wave profiles. These higher-order wave approximations offer a more accurate representation of real-world wave behavior, where increased crest elevations and asymmetrical shapes are critical for understanding hydrodynamic loads on structures.

Since we are interested in wave motion underneath a solid boundary, we subsequently turn to Stokes second problem, which describes the fluid motion induced by an oscillating rigid plate over a stationary fluid. The in-plane oscillatory motion of the plate influences the fluid near the fluid-structure interface, generating flow patterns that directly respond to the plate's movement and the formation of a laminar oscillating boundary layer, or Stokes Boundary Layer (SBL). However, our study diverges from this standard configuration by applying what is known as inverse forcing. Instead of a moving plate above a stationary fluid, we impose an oscillating flow that interacts with a stationary boundary, above. This modification alters the reference frame, fundamentally

changing the resulting flow dynamics. Such a configuration also represents real-world scenarios where flow near a bottom boundary is subjected to oscillations from above, such as tidal currents or wave-driven flows over the seabed. In such cases, oscillatory forces exerted by seiching, or standing wave oscillations, have been shown to significantly influence wave bottom boundary layer dynamics. Thus, based on Stokes second problem formulation, an *inverse* SBL framework has been proposed by Lorke et al. (2002) and has been used by subsequent studies in similar configurations (e.g., Jabbari and Boegman, 2021; Mellor, 2002).

In our study, a wave boundary layer is induced by propagating surface waves, driving cyclic variations in flow speed and direction underneath a stationary boundary. To describe this behavior quantitatively, we adopt a modified version of the above described inverse SBL framework, which is better suited for analyzing oscillatory boundary-layer flows under a flexible floating structure. Specifically, rather than just accounting for the general hyperbolical velocity decay with depth, we refine the approach by explicitly using either linear or higher-order SWT to capture the velocity decay more accurately for our wave conditions. This decay arises as wave-induced oscillatory motion decreases with increasing distance from the interface. Second, we incorporate the flexibility of the stationary boundary, as the "wall" in our setup does not remain rigid but dynamically responds to oscillatory forcing. This flexibility alters the effective boundary conditions, introducing additional complexities in near-wall flow dynamics. By integrating these modifications into the established SBL framework, we extend its applicability beyond rigid-boundary conditions, enabling a more accurate representation of boundary layer dynamics under wave forcing. This approach allows us to capture the essential flow characteristics while accounting for both velocity decay with depth and the dynamic response of the boundary. The following subsection provides the relevant formulas used to describe these modifications in detail, including the Stokes-wave expressions adopted in this study.

2.3. Adapted Stokes model

Starting with free surface waves, the horizontal velocity profiles for first-, second-, and third-order Stokes waves under free-surface conditions are given by Dean (1990), Stoker (1947):

$$U^{(1)}_{H,\text{Stokes}}(x,z,t) = a\omega\frac{\cosh[k(z+d)]}{\sinh(kd)}\cos\theta \tag{1}$$

$$U^{(2)}_{H,\text{Stokes}} = U^{(1)}_{H,\text{Stokes}} + \frac{3}{4}a\omega\, ak\frac{\cosh[2k(z+d)]}{\sinh(kd)^4}\cos 2\theta \tag{2}$$

$$U^{(3)}_{H,\text{Stokes}} = U^{(2)}_{H,\text{Stokes}} + 3a\omega\, A_{33}\,(ak)^2\frac{\cosh\big(3k(z+d)\big)}{\sinh^7(kd)}\cos 3\theta \tag{3}$$

with the third-order correction coefficient A_{33} defined as (Zhao and Liu, 2022):

$$A_{33} = \frac{9-4\sinh^2(kd)}{64\sinh^7(kd)} \tag{4}$$

Here, $\theta = kx - \omega t$ is the phase angle, $\omega = \frac{2\pi}{T}$ the angular frequency, $k = \frac{2\pi}{\lambda}$ the wave number, and $a = \frac{H}{2}$ the wave amplitude.

When a solid boundary is present, the classical Stokes second problem describes the flow generated by a rigid wall oscillating in-plane with a velocity:

$$U_{\text{wall}}(t) = U_0\cos(\omega t), \tag{5}$$

where U_0 is the amplitude of the wall velocity. This yields a velocity field that decays with distance from the wall, forming a laminar oscillatory boundary layer or SBL.

The analytical solution for the fluid velocity profile in this case is:

$$\hat{U}(z,t) = U_0 e^{-\kappa z}\cos(\kappa z - \omega t), \tag{6}$$

where $\kappa = \sqrt{\omega/2\nu}$, and ν is the kinematic viscosity of the fluid.

As mentioned earlier, the SBL approach above has been modified to describe cases of inverse forcing, i.e. oscillatory flows and wave-driven currents close to a stationary solid boundary, for example over the seabed (Lorke et al., 2002). The inverse forcing scenario is modeled by transforming the reference frame to move with the structure and subtracting the theoretical wave-induced velocity from the classical solution, which is valid under the linear Stokes boundary layer assumptions for small-steepness waves. Thus, U_0 in Eq. 6 no longer originates from wall motion, as in the classical case, but represents the horizontal velocity amplitude at the fluid-structure interface, as predicted by STW, in the absence of a boundary layer. We further adapt the above framework, for the case of an overlying solid boundary, fixed in the horizontal direction but allowed to move vertically over an oscillating flow beneath it, due to wave-induced velocities.

To account for the local inclination of the flexible structure, we approximate the boundary locally as a short, slightly sloped segment of a simple wave:

$$\eta(x,t) = a\cos(kx - \omega t).$$

From this wave representation, the spatial derivative, i.e. the local slope, and the corresponding angle, ϕ, with respect to the horizontal are given by:

$$\frac{\partial \eta}{\partial x}(x,t) = -ak\ \sin(kx-\omega t).$$

$$\phi(x,t) = \arctan\left(\frac{\partial \eta}{\partial x}(x,t)\right) = \arctan\big(-ak\ \sin(kx-\omega t)\big).$$

Because Stokes second problem (the classical oscillatory boundary layer) is formulated only in terms of tangential (horizontal) velocity, our analysis likewise focuses on the horizontal component. The vertical velocity is present in both measurements and STW, but is not part of the original Stokes boundary layer solution, and is therefore excluded when comparing with this theoretical framework. In order to then project the velocity onto the horizontal axis, we simply retain $\cos\phi(x,t)$ as our correction factor:

$$\cos\phi(x,t) = \frac{1}{\sqrt{1+\left(\frac{\partial \eta}{\partial x}\right)^2}} = \frac{1}{\sqrt{1+(ak\ \sin(kx-\omega t))^2}}.$$

This factor equals 1 at crests and troughs and reaches its minimum at zero crossings. Combining this correction with the inverse forcing formulation yields the adapted horizontal velocity profile:

$$U_H^*(x,z,t) \ = \ \hat{U}(z,t)\cos\phi(x,t) \ - \ U^{(X)}_{H,\mathrm{Stokes}}(x,z,t), \tag{7}$$

where $U^{(X)}_{H,\mathrm{Stokes}}(z,t)$ denotes the Stokes horizontal velocity of order X (second or third order in this study). The inclination correction enters through a cosine projection, whose minimum occurs at the zero-crossings and is set by the maximum interface slope; for a sinusoidal representation $\max|\partial\eta/\partial x| = ak = \pi(H/\lambda)$. For the present wave cases, the corresponding maximum reduction $1-\cos\phi_{\min}$ remains small, ranging from approximately 0.2% (W3-2/W5-2) to 0.5% (W6-2) and up to 2% (W3-3/W5-3), with the largest local tilt reaching $\phi = 11.5°$ ($\cos\phi_{\min} = 0.98$). This correction is nevertheless applied so that the adapted formulation remains directly comparable to the classical theory.

Thus, while the step implemented in Eq. (7) follows methodologies for oscillatory bottom boundary layers (Lorke et al., 2002), it is adapted here for near-surface flows beneath compliant structures like floating sea ice or marine infrastructure. The adaptations introduced in this study are twofold: (i) inclusion of a $\cos\phi(x,t)$ factor to account for the phase-dependent inclination of the flexible interface, and (ii) use of the corresponding $U^{(X)}_{H,\mathrm{Stokes}}(x,z,t)$ profile for the specific wave order, rather than the simple sinusoidal forcing with no decay typically used in bottom boundary layer models. This formulation will hereafter be referred to as the adapted Stokes model (ASM).

2.4. Boundary layer thickness

To quantify the effect of the flexible structure on the near-surface flow, we focus on the boundary layer that forms beneath the interface. The characteristic penetration depth of this oscillatory boundary layer, often referred to as the Stokes layer depth ($=\sqrt{2\nu/\omega}$) (Sana and Tanaka, 2007), defines the region over which the velocity decays significantly from the interface. In some studies, an alternative definition of the SBL thickness has been proposed (Ronald and Panton, 2013; Coxe et al., 2022, 2024):

$$\delta_{\mathrm{Stokes}} = 4.6\sqrt{\frac{2\nu}{\omega}}, \tag{8}$$

which corresponds to the depth at which the oscillatory velocity decreases to approximately 1% of its surface value, an intuitively observable threshold that simplifies comparison between theoretical predictions and measurements, rather than the e^{-1} decay length used in the classical definition of the Stokes penetration depth (Berumen and Goree, 2021; Akhavan et al., 1991).

For laminar oscillatory flows, another analytical expression for the boundary layer thickness is given by Jensen's laminar correction (Jensen et al., 1989):

$$\delta_L = \frac{3\pi}{4}\sqrt{\frac{2\nu}{\omega}} \iff \frac{\delta_L}{a_m} = \frac{3\pi}{4}\left(\frac{2}{Re}\right)^{1/2} \tag{9}$$

where δ_L is the laminar wave boundary layer thickness, $Re = U_0 a_m/\nu$ is the wave Reynolds number, and $a_m = U_0/\omega$ is the maximum particle excursion length. Together, δ_{Stokes} and δ_L provide useful theoretical benchmarks for laminar oscillatory flows.

However, both of these classical scales are phase-independent and assume an idealized velocity decay, which may not hold near a compliant, moving boundary. To better capture local deviations, a data-driven definition of boundary layer thickness is required. A conventional approach defines the boundary layer thickness as the vertical position at which the local velocity differs by less than a certain threshold-typically 1% or 5%-from the free-stream velocity. In steady flows, this definition is relatively straightforward. In oscillatory boundary layers, however, the velocity varies with depth not only in magnitude but also in shape, making this definition more nuanced (Sana and Tanaka, 2007; Sleath, 1987; Yuan and Madsen, 2014). These complexities are particularly relevant when wave motion interacts with a deformable boundary, where additional fluid-structure interactions influence the near-surface velocity field.

In this study, we define the wave boundary layer thickness, denoted as $\delta_{5\%}$, as the distance from the fluid-structure interface to the point where the measured horizontal velocity $U_{\text{exp}}(z)$ deviates by more than 5% from the estimated free-stream velocity $U_\infty(z)$:

$$\left| \frac{U_{\text{exp}}(z) - U_\infty(z)}{U_\infty(z)} \right| = 0.05$$

Although both 1% and 5% criteria are used in literature, the 5% threshold was chosen here due to the spatial resolution limitations of the PIV system and the relatively small velocity gradients beyond the boundary layer. This criterion provides a practical balance between sensitivity and robustness for tracking $\delta_{5\%}$ across the wave cycle.

The free-stream velocity $U_\infty(z)$ refers to the undisturbed horizontal velocity profile outside the boundary layer, where the flow is no longer affected by viscosity. In theory, this velocity decays exponentially with depth according to:

$$U_\infty(z) = U_0 e^{-kz},$$

where U_0 is the velocity amplitude at the interface. Here, z is zero at the free surface and increases downward, as illustrated in Fig. 1. In practice, $U_\infty(z)$ is estimated by fitting velocity data in the region beyond the boundary layer (i.e., for $z > \delta_{\text{Stokes}}$). While an exponential decay would be more theoretically consistent, the observed decay was sufficiently gradual that a linear approximation produced reliable results for extrapolation toward the interface.

This $\delta_{5\%}$ extraction method enables a phase-resolved estimate of boundary layer thickness and supports direct comparison with theoretical models. Analytical expressions such as δ_{Stokes} and δ_L provide useful benchmarks, but their phase-independent nature limits their ability to capture local deviations. Laminar corrections, such as Jensen's model (Jensen et al., 1989), provide alternative scaling under specific conditions. Other definitions, such as identifying the vertical position of maximum velocity overshoot beneath the crest, have been proposed for shallow or nonlinear wave conditions, but were not consistently observable in our experimental data and are less reliable across the wave cycle.

2.5. PIV data processing

The experimental facility, wave generation, PIV system configuration, and seeding procedure were described in Section 2.1. Here, we focus on the processing steps relevant to the present analysis.

Individual particle image pairs were obtained at multiple instances across each wave cycle (including sufficient overlap) and were phase-locked to the wave probe signal, so that they could be associated with the appropriate wave phase. The overlap extent varied by wave case, corresponding to about 5% of a single camera frame (approximately 4.5 mm) for the longer waves (W3-2, W3-3) and up to 57% for shorter waves (W6-2), ensuring continuous coverage over one full wavelength.

Before further analysis, the region above the fluid–structure interface was masked in each image, using reflected laser light to identify the interface. Minor phase-to-phase variations in interface position were observed, with a maximum of 2.8 mm for the third-order wave case W3-3. This corresponds to about 2.5 % of the wave height, and is attributed to wave fluctuations and synchronization noise. Details of the masking procedure and uncertainty assessment are provided in Uksul et al. (2025). The masked image pairs were then processed to obtain PIV velocity vector fields; the corresponding analysis settings and acquisition parameters are reported in Section 2.1.

For each wave cycle, the synchronized, individual PIV vector fields were stitched together across their overlapping regions, in order to reconstruct the velocity field underneath a full wave cycle. The reconstructed fields were then averaged across all cycles within (the steady-state segment of) each run. For each wave case and experimental run, a minimum of 25 wave cycles were recorded, to ensure statistical convergence of first-order quantities, with variations stabilizing within ±5% in phase-averaged values. However, this ensemble size is not sufficient for robust higher-order fluctuation statistics, which generally require substantially larger ensembles in phase-locked experiments (Kearney et al., 2009).

All runs satisfied this threshold, each typically spanning 30 to 55 cycles; run-to-run variation of results was minimal (see also discussion in Appendix A). For further details on the experimental setup, data acquisition, and processing, the reader is referred to Uksul et al. (2025).

Fig. 2 illustrates the resulting phase-averaged velocity field for wave case W3-2 under free surface conditions, averaged over 30 wave cycles. The stitched field covers one wavelength with 3329×179 velocity vectors. The wave propagates from left to right, with x/λ denoting the normalized horizontal coordinate. The figure serves as a representative example of the velocity fields obtained in this study.

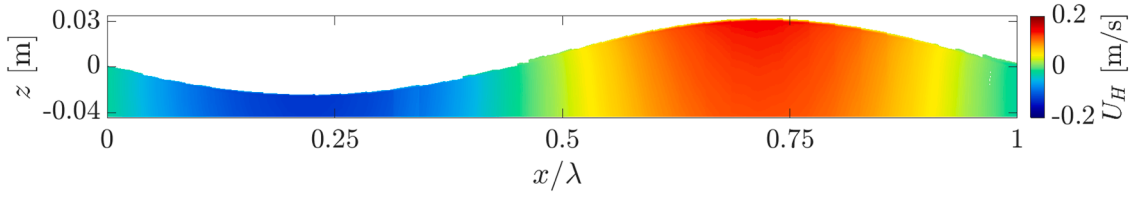

Fig. 2. Phase-averaged horizontal velocity field under free surface conditions for wave case W3-2, shown over one full wavelength. The field is constructed by stitching together sequential PIV measurement windows to cover the entire wave cycle.

From these averaged datasets, horizontal velocity profiles were extracted at specific wave phases (crest, trough, zero up-crossing, zero down-crossing) to highlight important stages of the wave-induced flow and enable consistent comparisons between different cases (see Fig. 3). The crest was defined as the highest point between a zero up-crossing and the following zero down-crossing, while the trough was the lowest point between a down-crossing and the next up-crossing. The velocity is normalized by U_0, and the vertical position by the wave amplitude $a = H/2$, consistent with the wave heights H listed in Table 3. The shaded area indicates the wave shape, with still water level (SWL) shown as a dashed line. The horizontal axis represents a composite view of the four characteristic phases, arranged sequentially for comparison. This visualization accentuates the differences in profile shape, since arranging the four phases sequentially around zero emphasizes local deviations. As a result, the mismatch with theory appears larger than it is in absolute terms, where the offsets from the theoretical velocity remain small compared to the overall velocity scale.

Following the profile extraction, horizontal velocity profiles were further smoothed by averaging across two interrogation windows (IWs) in the streamwise direction. This step reduced local fluctuations and improved the clarity of velocity gradients near the interface. Since the wavelength is much larger than the horizontal extent of the IWs, this procedure does not significantly average out spatial gradients; adjacent values are expected to be nearly identical.

All velocity data presented in the following sections are based on the process of stitching, averaging and profile extraction as described above. This approach minimizes random variability and enables characterization of near-surface velocity structure across wave phases, wave steepnesses, and structural configurations. For consistency, both wave elevation and PIV measurements are reported at Pos1 for all cases, with the exception of wave case W6-2, where additional measurements at Pos2 are presented to quantify wave attenuation as the wave propagates beneath the structure.

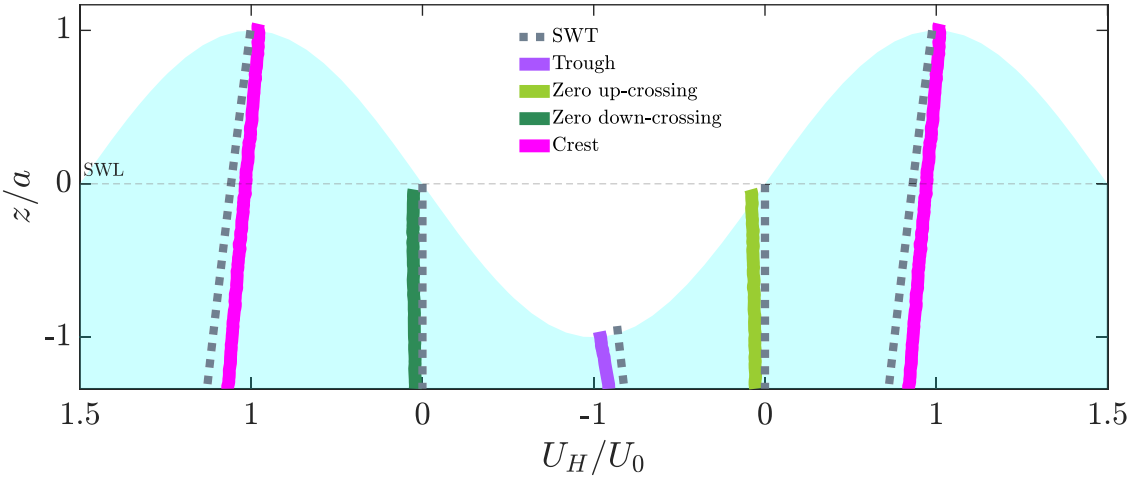

Fig. 3. Phase-resolved horizontal velocity profiles U_H/U_0 for wave case W3-2 under free surface conditions. Experimental data are compared with second-order Stokes wave theory. Velocity is normalized by U_0, and vertical position by a. The shaded area indicates the wave shape, with SWL shown as a dashed line. The horizontal axis represents a composite view of four characteristic wave phases (crest, trough, zero up-crossing, and zero down-crossing), arranged sequentially for comparison. This visualization accentuates the differences in profile shape, but also makes the apparent mismatch look larger than in absolute terms, since the offsets from zero velocity are small relative to the normalization scale.

3. Results and discussion

3.1. Second order waves

We start the results discussion with second order waves of low steepness ($H/\lambda = 0.02$) and varying wavelength, corresponding to wave cases W3-2 and W5-2 (see also Table 3). Focusing first on wave W3-2, two experimental configurations were considered: waves propagating under free surface conditions and beneath a continuous, flexible floating structure. Figs. 2 and 3, previously introduced in the Methods section to illustrate the measurement setup, depict the former and are now examined in the context of results, serving as a baseline reference for comparison with cases beneath the flexible structure.

The phase-averaged velocity field for wave case W3-2 under free surface conditions displays characteristic wave-induced behavior: horizontal velocities are highest near the surface, both at the crest and trough, and decrease with depth (Fig. 2). Although only the free surface case is shown, the corresponding velocity field under the flexible structure appears visually similar in terms of large-scale structure and is therefore not shown. The corresponding horizontal velocity profiles U_H/U_0 for the free surface case at four characteristic wave phases (crest, trough, zero up-crossing, and zero down-crossing) are then extracted and shown in Fig. 3. The shaded region illustrates the nominal wave shape at the respective phase, with the still water level (SWL) indicated by a dashed line. Experimental results are compared with second order SWT, which is valid for free surface conditions. The profiles show good agreement with the theoretical predictions in terms of velocity magnitude and decay with depth across all phases. The largest deviation, approximately 6%, is observed at the trough, relative to the theoretical velocity magnitude predicted for that phase.

We now move to the velocity fields of the second configuration, where a flexible boundary is present on top of the free surface, for the same wave condition (W3-2). Fig. 4 presents the horizontal velocity U_H profiles at the same characteristic wave phases as above. Away from the fluid-structure interface, the experimental velocity aligns closely with the theoretical prediction based on ASM second order Stokes theory, with minor differences, notably a slight overprediction near the trough. This overall agreement is very similar to what was observed under free surface conditions, indicating that in the bulk of the flow, the presence of the structure does not significantly alter the large-scale velocity distribution. Close to the interface, ASM predicts a small velocity overshoot, a feature typical of oscillating boundary layers (Nielsen, 1992), which is also visible in the experimental data for most phases. The agreement is particularly good at the crest and trough locations.

However, at the zero-crossing phases, the experimental data show significantly lower overshoot magnitudes than predicted. Given that the boundary layer thickness is on the order of mm, this discrepancy is not unexpected: such sharp velocity gradients are difficult to resolve accurately with PIV, especially near regions of rapid acceleration or sign change, where phase-averaging can further amplify the influence of cycle-to-cycle variations and measurement uncertainties (Keane and Adrian, 1990).

A second wave case, wave W5-2, is shown in Fig. 4, bottom panel. It has a shorter wavelength than W3-2, but the same wave steepness of ($H/\lambda = 0.02$). Horizontal velocity profiles are shown for the same four wave phases as before, with experimental data compared to predictions from the ASM. The model reproduces the overall velocity structure well. The largest deviation is observed at the trough, where the overshoot in the experimental profile is again less pronounced than predicted. At the zero-crossing phases, the experimental data also underestimate the overshoot relative to theory, similar to observations for W3-2.

Having established the velocity field behavior from PIV measurements, we now turn to complementary wave probe (WP) data for wave case W3-2. These provide independent insight into the surface elevation and harmonic composition, allowing direct comparison with theoretical wave profiles. Fig. 5 shows the phase-averaged surface elevation and corresponding frequency spectrum for wave case W3-2, obtained from wave probe measurements under free-surface conditions and beneath the flexible structure. The wave profile is slightly asymmetric compared to the linear reference case, consistent with the behavior of a second-order Stokes wave. This asymmetry is characterized by a sharpened crest and a broader trough. A direct comparison of the flexible-structure wave probe

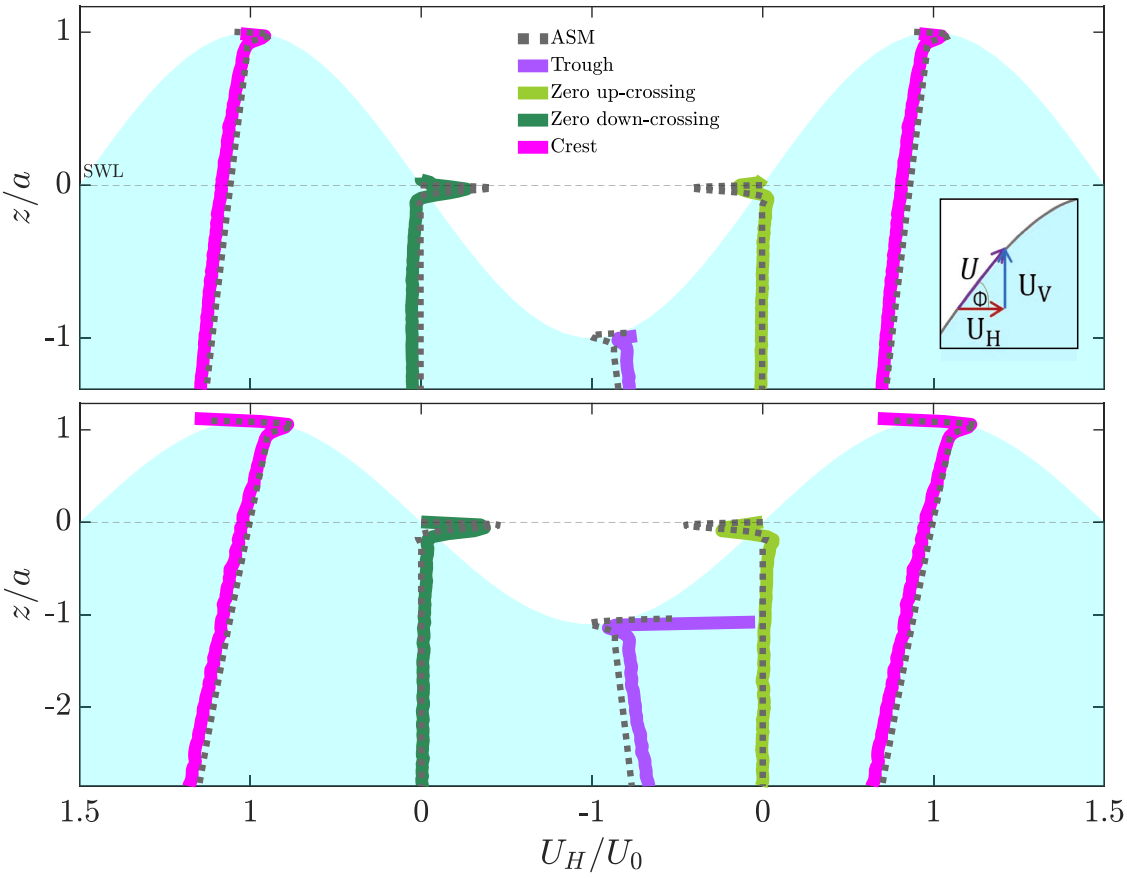

Fig. 4. Phase-resolved horizontal velocity profiles U_H/U_0 under the flexible structure for two wave cases. Top: W3-2 (longer wavelength); bottom: W5-2 (shorter wavelength). Both have the same steepness but differ in wavelength. Experimental data are compared with predictions from the ASM. Velocity is normalized by U_0, and vertical position by a. The shaded area represents the wave shape, SWL is indicated by a dashed line. An inset schematic defines the local interface tilt angle ϕ and the corresponding decomposition of the velocity components used in the ASM.

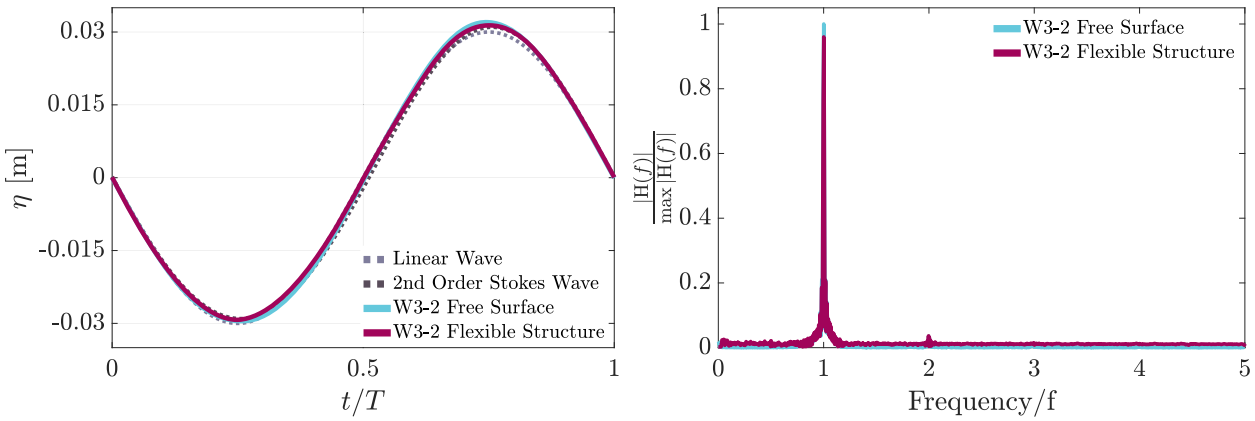

Fig. 5. Phase-averaged wave elevation and normalized frequency spectrum for wave case W3-2. Left: comparison of surface elevation under free surface and flexible structure conditions with linear and 2nd order Stokes wave theory. Right: corresponding FFTs showing harmonic content.

signal with the theoretical second-order Stokes profile shows the largest discrepancy near the zero crossing, 1.97 mm, corresponding to approximately 3.3% of the wave height ($H = 60$ mm). The corresponding FFT reveals a dominant peak at the wave frequency (0.714 Hz, corresponding to a wave period of 1.4 s), along with a small second harmonic component, in line with theoretical expectations for low wave steepness. This same wave case (W3-2) was also examined in our earlier study (Uksul et al., 2025), where attenuation and boundary layer effects were discussed but overshoot dynamics could not be resolved due to limited spatial resolution. The present measurements extend that analysis by directly resolving the near-interface velocity structure and boundary layer characteristics.

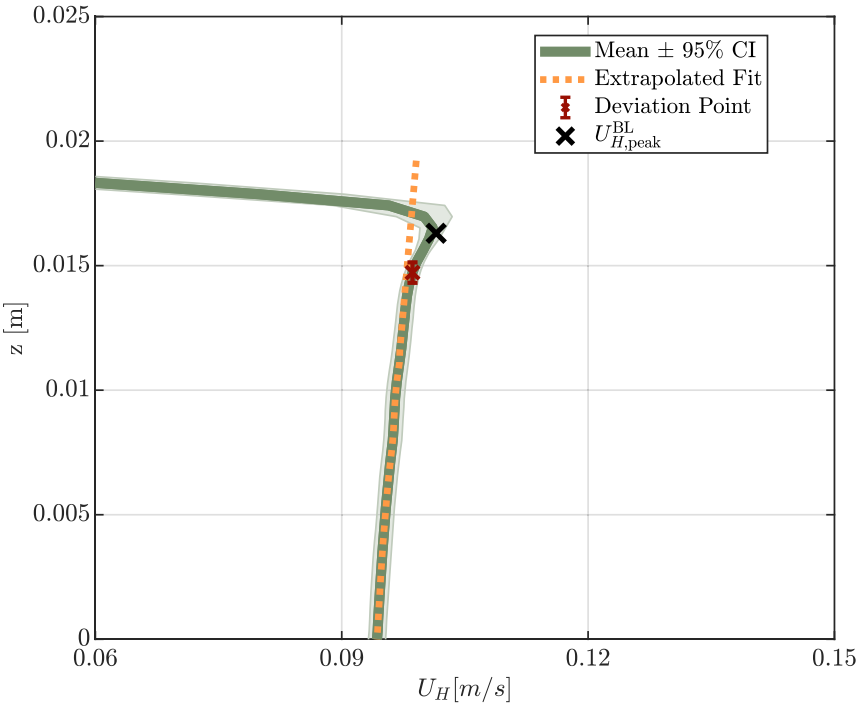

Fig. 6. Example of boundary layer peak detection from an experimental horizontal velocity profile U_H. The solid curve shows the phase-averaged profile for one representative case; the shaded band indicates the 95% confidence interval of the mean profile based on wave-to-wave variability within the same run ($N = 30$). The extrapolated free-stream fit and detected deviation point are shown, and the black cross marks the identified peak velocity within the boundary layer, $U_H^{\mathrm{BL,peak}}$.

The horizontal velocity profiles presented in the previous sections reveal a near-interface overshoot, characteristic of oscillatory boundary layers. To further quantify this, two parameters were extracted from the experimental profiles: the boundary layer thickness

$\delta_{5\%}$ and the peak horizontal velocity within the boundary layer $U_H^{\mathrm{BL,peak}}$. Fig. 6 illustrates an example of this detection process for a single phase-averaged velocity profile.

To provide a transparent indication of experimental repeatability at the profile level, the same figure also includes uncertainty bounds based on wave-to-wave variations within the run: the shaded region represents the 95% confidence interval of the mean profile computed from repeated wave realizations at the same phase. The spread is largest close to the interface, where small run-to-run variations in the instantaneous interface elevation and masking lead to the strongest apparent variability. A broader set of profiles with corresponding confidence bands across wave phases and representative cases is provided in Appendix A.

The boundary layer thickness $\delta_{5\%}$ is defined as the vertical distance from the fluid–structure interface to the location where the experimental profile begins to deviate by more than 5% from the extrapolated free-stream velocity. To estimate the free-stream behavior, a linear fit is applied to the bulk region of the profile, well below the interface where boundary layer effects are negligible, and extended toward the interface. The boundary layer edge is then identified as the point where the measured velocity diverges from this extrapolated fit by more than 5%. The peak horizontal velocity $U_H^{\mathrm{BL,peak}}$ is identified as the maximum value within this boundary layer region. These two parameters provide a practical means of characterizing the wave boundary layer and its deviation from theoretical expectations.

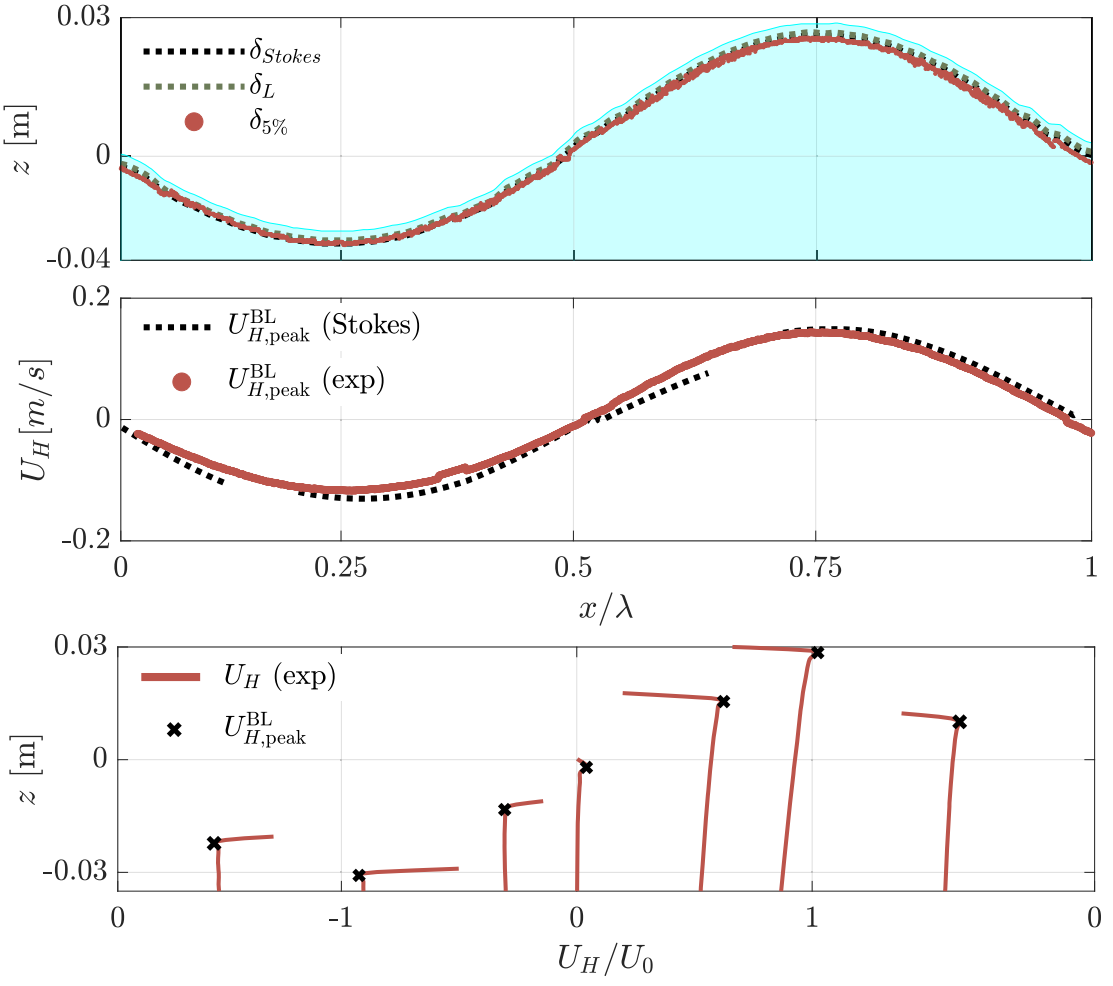

Fig. 7. Boundary layer thickness and peak velocity for wave case W3-2 under the flexible structure. Top: experimental boundary layer thickness $\delta_{5\%}$ based on a 5% velocity threshold, compared with δ_{Stokes} and the laminar boundary layer prediction δ_L from Jensen et al. (1989) Middle: horizontal velocity at the peak location of the boundary layer U_H^{BL}, from experiments and the ASM. Bottom: example experimental profiles of U_H with detected peak locations U_H^{BL} marked by ×.

Fig. 7 presents the extracted boundary layer thickness $\delta_{5\%}$ and corresponding peak velocity magnitudes over the wave cycle for case W3-2 under the flexible structure. The top panel shows the experimentally determined boundary layer thickness $\delta_{5\%}$ over one full wavelength for wave case W3-2 under the flexible structure. Two theoretical estimates are included for reference: the laminar thickness from Jensen et al. (1989), $\delta_L = 1.62$ mm, and the scaled Stokes thickness $\delta_{\mathrm{Stokes}} = 3.15$ mm, which corresponds to the 1% criterion ($U/U_0 = 0.01$). Both estimates are phase-independent and depend only on fluid properties and wave period. The experimental

values for $\delta_{5\%}$ remain relatively constant at approximately 3 mm throughout the wave cycle and align closely with the prediction based on δ_{Stokes}, while δ_L underestimates the boundary layer thickness. This supports the applicability of Stokes' laminar boundary layer theory in low-steepness wave conditions.

The middle panel of Fig. 7 shows the peak horizontal velocity within the boundary layer, $U_H^{\text{BL,peak}}$ for both the experimental results and the ASM. Agreement is good near the wave crest but diverges around the trough and close to the zero-crossing phases. In the theoretical results, gaps appear shortly after the zero-crossings due to a phase lag in the boundary layer response, during which two distinct peaks may occur, making the true maximum ambiguous. This feature is not seen in the experimental data, likely because the spatial resolution of PIV is insufficient to resolve multiple close velocity peaks near the interface.

The bottom panel shows selected horizontal velocity profiles from the experimental data, providing examples of how $U_H^{\text{BL,peak}}$ was identified at different wave phases.

These results indicate that for waves of moderate steepness and wavelength, the ASM formulation provides a reliable estimate of the horizontal velocity distribution and boundary layer development beneath a compliant surface. The remaining deviations, primarily at the zero-crossing phases, can be attributed to experimental limitations in resolving sharp gradients within the narrow boundary layer.

3.2. Attenuating second order waves

Here, the focus is on wave case W6-2, characterized by a wavelength of approximately 0.66 m and a steepness of $H/\lambda = 0.033$. Compared to the previous two cases, W6-2 features both a shorter wavelength and a markedly increased steepness (see Table 3). While the wave remains within the second order regime in terms of frequency content and overall shape, it exhibits enhanced nonlinearity, which can influence both the velocity field and boundary layer development beneath the flexible structure.

Fig. 8 shows the U_H at different wave phases under the flexible structure. In contrast to the previous second order cases, the experimental data now diverge more noticeably from the theoretical predictions. The mismatch is particularly evident at the wave crest and trough, where the slope of velocity decay with depth deviates from that predicted by the ASM. The predicted boundary layer is thin, with steep velocity gradients that challenge PIV resolution. With an expected thickness of $\delta_{\text{Stokes}} = 2.15$ mm, it falls below the spatial resolution needed to consistently resolve its evolution throughout the wave cycle.

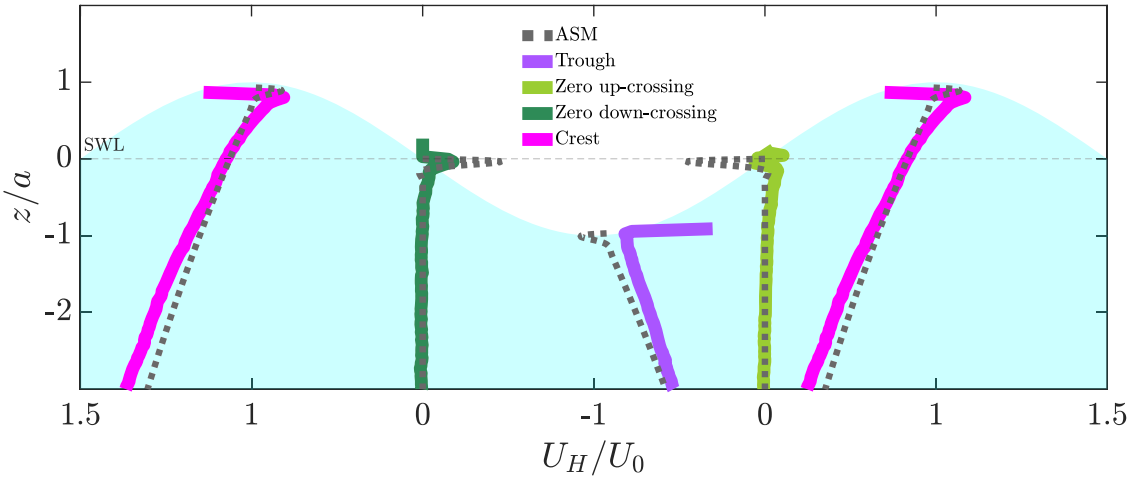

Fig. 8. Phase-locked horizontal velocity profiles U_H/U_0 at four wave phases for wave case W6-2 under the flexible structure. Experimental results are compared with the ASM. Velocity is normalized by local crest velocity U_0, and vertical position is scaled by a.

As shown in Uksul et al. (2025), attenuation was expected for this wave case (W6-1 in that study), and the present results confirm this behavior. Fig. 9 displays the phase-averaged surface elevation and corresponding frequency spectra, with wave probe locations indicated in Fig. 1. While the initial waveform under free surface conditions (measured at Pos1) exhibits the expected sharp crest and broader trough, subsequent profiles beneath the flexible structure show a clear reduction in a. The crest height decreases from 11.9 mm at the free surface to 9.9 mm at Pos1 (a reduction of 16.7 %), and further to 7.1 mm at Pos2, corresponding to a total attenuation of 40.8 %. This behavior is consistent with earlier observations of attenuation for the same wave under a compliant cover (Uksul et al., 2025), and is in line with previous studies showing that shorter and steeper waves undergo stronger damping beneath floating structures (Sree et al., 2018; Sutherland et al., 2017; Schreier and Jacobi, 2021b). Nevertheless, the wave shape in both positions continues to exhibit second-order characteristics, with no significant distortion in the harmonic composition as confirmed by the FFT.

Further insight into the boundary layer behavior is provided in Fig. 10, where the horizontal velocity at the wave crest is plotted for both Pos1 and Pos2, normalized by the local surface velocity amplitude U_H/U_0. The present dataset contains only these two streamwise locations, which are separated by 4 m. When normalized, the velocity profiles align closely, indicating that both the overshoot magnitude and the boundary layer thickness scale proportionally with the local wave forcing. This suggests that, despite

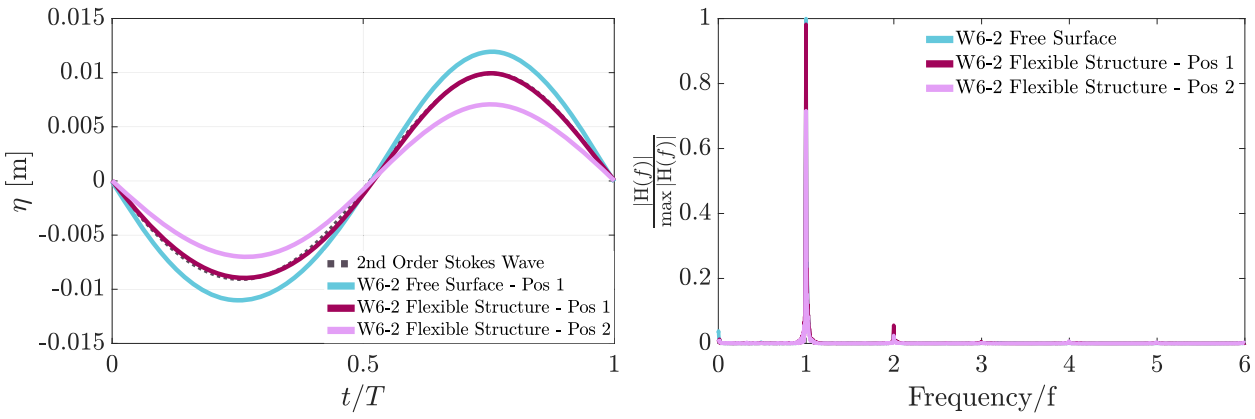

Fig. 9. Phase-averaged wave elevation and normalized frequency spectrum for wave case W6-2. Left: surface elevation at the free surface, and under the flexible structure at Pos 1 and Pos 2, compared with second order Stokes theory. Right: corresponding FFTs showing the spectral content at each location.

the attenuation of the wave as it travels under the flexible structure, the boundary layer dynamics remain approximately similar between Pos1 and Pos2; potential edge effects were not assessed in this dataset.

Overall, while the steepness and short wavelength introduce measurement challenges and increase deviation from theoretical predictions, the underlying structure of the boundary layer appears to scale predictably with a. The results highlight both the limitations of optical measurement techniques at small boundary layer scales and the robustness of the normalized boundary layer behavior under wave attenuation.

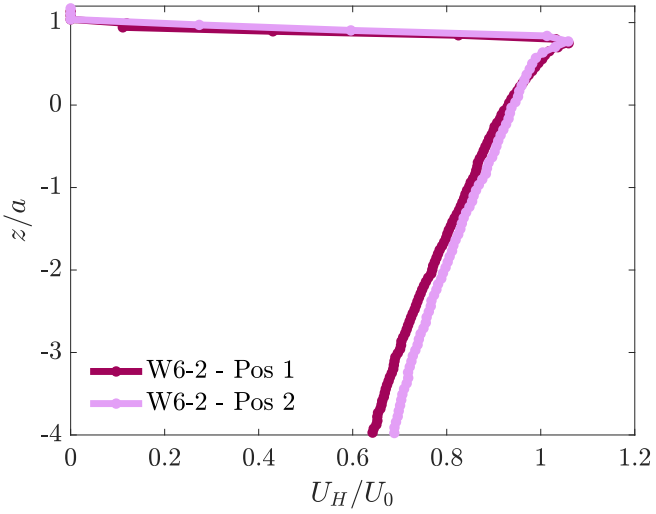

Fig. 10. Normalized horizontal velocity profiles U_H/U_0 at the wave crest for wave case W6-2 at the two available PIV measurement locations along the flexible structure (Pos1 and Pos2, separated by 4 m). Velocity is normalized by U_0, and vertical position is scaled by a.

3.3. Third order Stokes waves

Third-order Stokes theory extends the classical wave description by incorporating higher-order nonlinearities, capturing effects that second-order models cannot. These include waveform asymmetry, with sharper crests and broader troughs compared to second-order waves, which retain more symmetry in their shape. The inclusion of third harmonics in the velocity potential and free-surface elevation equations enables more accurate representation of steep, nonlinear waveforms commonly encountered in real ocean conditions and in laboratory experiments involving finite-amplitude waves. Among the present cases, W3-3 (and later W5-3) fall into this regime, as indicated in Table 3, making third-order theory the appropriate reference.

Fig. 11 illustrates the time-averaged wave profile for case W3-3 under both free-surface and flexible-structure conditions. In free-surface conditions, the waveform shows the expected third-order characteristics: a narrow, steep crest and a more extended trough. Beneath the flexible structure, however, the wave shape is further modified. The crest height increases slightly from 110.9 mm (third-

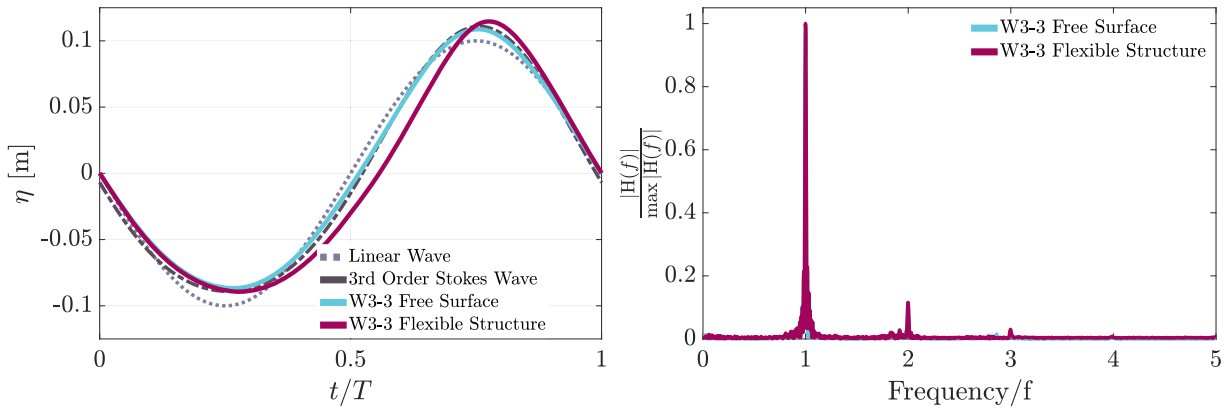

Fig. 11. Phase-averaged wave elevation and normalized frequency spectrum for wave case W3-3 under free surface and flexible structure conditions. Left: time series of surface elevation compared with linear and third-order Stokes wave theory. Right: corresponding FFT showing harmonic content.

order Stokes) to 114.6 mm (an increase of 3.34 %), while the zero crossing is delayed from $t/T = 0.523$ to $t/T = 0.55$, corresponding to a relative shift of approximately 5.2 %. These changes indicate a sharper crest and a broadened trough, signatures of enhanced harmonic distortion due to wave-structure interaction. The corresponding FFT (Fig. 11) confirms this interpretation: distinct peaks appear at the fundamental frequency and its second and third harmonics, demonstrating the strong nonlinear character of the surface displacement signal.

These changes in wave shape are not merely superficial. They directly impact the subsurface flow and the formation of the wave-induced boundary layer. In the top subplot of Fig. 12, the boundary layer thickness δ_{BL} detected beneath the crest region of W3-3 is shown. The experimental boundary layer thickness, $\delta_{5\%}$, is consistently greater than the theoretical prediction based on the ASM formulation ($\delta_{\mathrm{Stokes}} = 3.15$ mm), which assumes linear, oscillatory flow driven by wave theory. Experimentally determined $\delta_{5\%}$ values varied with wave phase, reaching up to approximately 7 mm near the rising flank close to the zero crossing (about 40% greater than the theoretical value), while at the crest they were in reasonable agreement with the prediction. Consistent with this observation, the

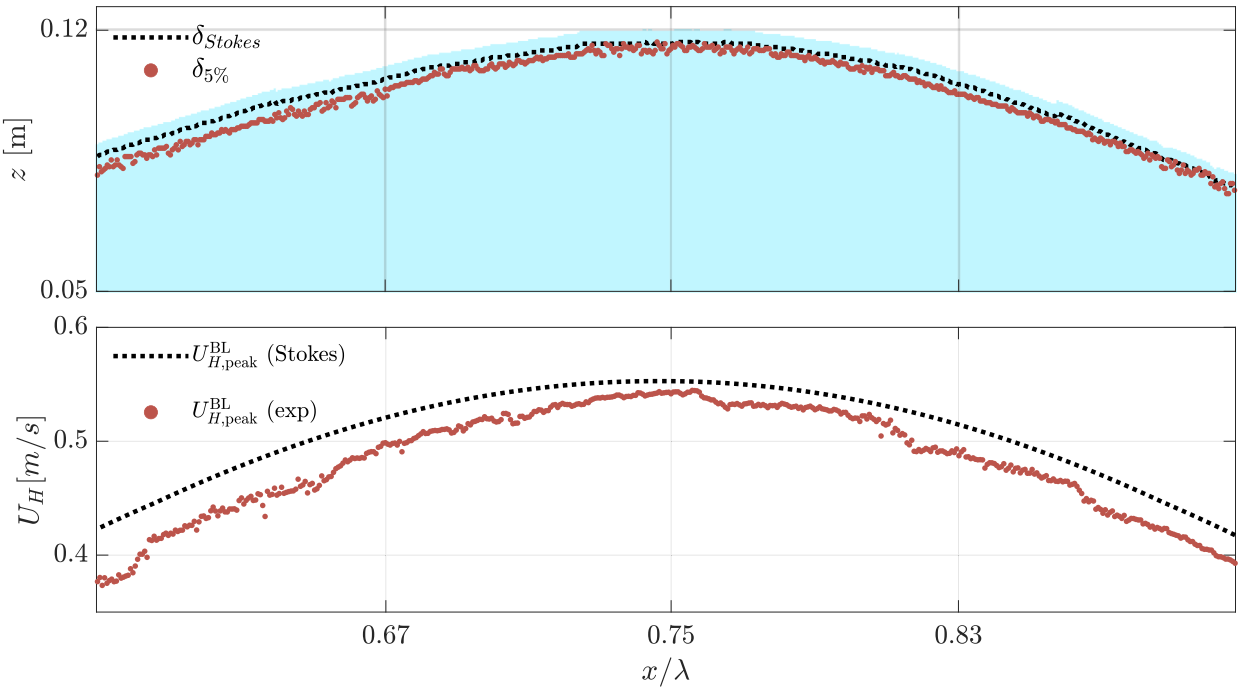

Fig. 12. Boundary layer thickness and peak velocity for wave case W3-3 under the flexible structure. Top: experimental boundary layer thickness $\delta_{5\%}$ compared with the predicted boundary layer depth δ_{Stokes} from the ASM. Bottom: horizontal velocity at the boundary layer peak U_H^{BL} from experiments and the ASM. Data is shown for the crest region of the wave cycle.

largest model–data mismatch occurs near the zero-crossing phases. This discrepancy suggests enhanced momentum transport near the compliant interface, potentially driven by structural oscillations or induced shear instabilities.

The inclination (cosine) projection in the ASM cannot explain these discrepancies: even for the steepest cases considered here the maximum reduction $1 - \cos\phi_{\min}$ is only on the order of 2% (Section 2.3), whereas the observed deviation in $\delta_{5\%}$ is substantially larger. This indicates a breakdown of the underlying simplifications of the ASM under high steepness/third-order conditions. A likely failure path is the increased role of non-tangential and nonlinear kinematics near the zero-crossings, where the interface slope is maximal. Under these conditions, strong curvature and vertical acceleration can produce local adverse pressure gradients that are not represented by the laminar boundary layer formulation.

The bottom subplot of Fig. 12 shows $U_H^{\mathrm{BL,peak}}$. Here, the ASM significantly overpredicts the magnitude of the overshoot, especially near the wave crest. This may be attributed to the breakdown of assumptions underlying the model, specifically, the neglect of energy dissipation mechanisms such as viscous damping, turbulence, or flow separation triggered by surface curvature and vertical accelerations (Bettencourt and Dias, 2018; Schlichting and Kestin, 1961; You et al., 1992).

Further insights can be drawn from Fig. 13 , which compares horizontal velocities at the crest location for W3-3 and W5-5. Despite the increased steepness in W3-3 and W5-3, the same trend holds: the experimentally measured BL thickness exceeds theoretical estimates, while the overshoot velocity remains consistently lower than predicted. This robustness across wave cases strengthens the interpretation that the classical theory, while useful in regimes of weak nonlinearity, fails to capture critical dynamics under strong wave-structure interaction.

Taken together, these observations underscore the limitations of purely linear models for predicting near-interface boundary layer behavior under realistic wave forcing. Third-order wave components not only reshape the surface profile but also drive significant deviations in subsurface flow, especially under compliant boundaries. Future modeling efforts should consider incorporating nonlinear effects, structural feedback, and potential onset of turbulence to better resolve the complex fluid-structure interactions observed experimentally.

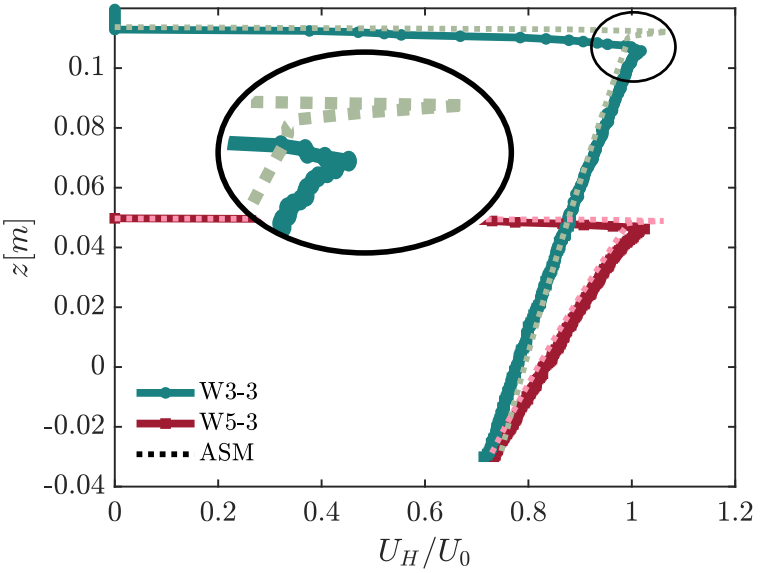

Fig. 13. Normalized horizontal velocity profiles U_H/U_0 at the wave crest for wave cases W3-3 and W5-3. Experimental results are shown alongside predictions from the ASM. A zoomed-in view of the boundary layer for W3-3 highlights the discrepancies between experimental data and the model.

4. Conclusion

This study presents a detailed experimental investigation of wave-induced boundary layer formation beneath a continuous, flexible floating structure. The results confirm the existence of a distinct near-surface boundary layer, with the flexible structure primarily affecting the flow in close proximity to the fluid–structure interface. This influence decays rapidly with depth, suggesting that the structure's impact is confined to the near-interface region rather than inducing widespread alterations in the flow field.

Under long, low-steepness wave conditions, the experimental velocity profiles show good agreement with both second-order wave theory and an adapted Stokes boundary layer model. This agreement holds true beneath the structure and in open water. In these cases, estimates of boundary layer thickness and overshoot magnitude are reasonably accurate, supporting the use of simplified laminar models under limited nonlinear conditions.

In contrast, steeper, short waves result in clear deviations between theory and experiment. ASM fails to capture the correct slope of the velocity profile near the interface, and overshoot estimates diverge. These wave conditions also exhibit attenuation beneath the structure, indicating additional energy dissipation mechanisms—potentially linked to nonlinear interactions (Xu and Guyenne, 2023),

convective acceleration, and incipient flow separation under surface curvature and vertical acceleration (National Research Council, 1994; Fielding et al., 2013).

Notably, for third-order wave conditions, the ASM remains effective away from the immediate interface region. Nonetheless, it consistently underestimates boundary layer thickness while overestimates the overshoot—highlighting the model's limitations in capturing fine-scale velocity gradients under increasing nonlinearity. These limitations are most evident near the zero-crossing phases, where the cosine projection remains small and the underlying ASM assumptions are most strained.

Fig. 14 provides a compact synthesis at the crest for three representative regimes: (i) long, low-steepness second-order waves (W3-2), (ii) shorter, attenuating second-order waves (W6-2), and (iii) third-order/high-steepness waves (W3-3). The insets highlight the near-interface boundary-layer/overshoot region, while the shaded bands indicate the 95% confidence interval of wave-to-wave variability within each run. Across the full dataset, agreement with ASM is strongest for low-steepness conditions and away from the immediate interface beneath the structure, whereas deviations increase with wave steepness and are most pronounced near the interface and around the zero-crossings, where the interface slope is maximal and the flow undergoes its most rapid sign change, placing the ASM assumptions under the greatest strain. Under attenuating conditions (e.g., W6-2), the wave forcing evolves along the structure, and additional dissipation mechanisms might further contribute to the observed departures from the simplified laminar prediction.

These results emphasize the need for refined theoretical models that account for nonlinear wave effects and structural compliance more accurately. They also underscore the importance of high-resolution experimental data in validation of such models.

Beyond model development, the present data provide directly usable quantitative benchmarks for dissipation/attenuation parameterizations under floating covers. For VLFS applications, the measured boundary layer thickness range quantifies the near-interface region where velocity gradients concentrate and therefore provides a parameter required in design-oriented hydrodynamic models.

These measurements also provide quantitative inputs for boundary layer-based attenuation models used for floating covers and sea-ice analogues: inextensible cover theories attribute wave-energy decay to dissipation in an oscillatory boundary layer generated at the interface (e.g., Sutherland et al., 2017; Sree et al., 2018). In this context, the experimentally determined boundary layer thickness (e.g. $\delta_{5\%} = 3.15$–7 mm depending on case and phase) can be used as validation for such parameterizations, alongside the effective attenuation inferred from the measurements for W6-2.

Future work should explore coupling viscous modeling with wave–structure interaction frameworks to better resolve the dynamics near compliant boundaries, particularly for offshore applications involving floating energy systems or large-scale flexible structures. Future experiments could target higher near-interface resolution through a dedicated optical arrangement or complementary point measurements (e.g., LDV) where access permits.

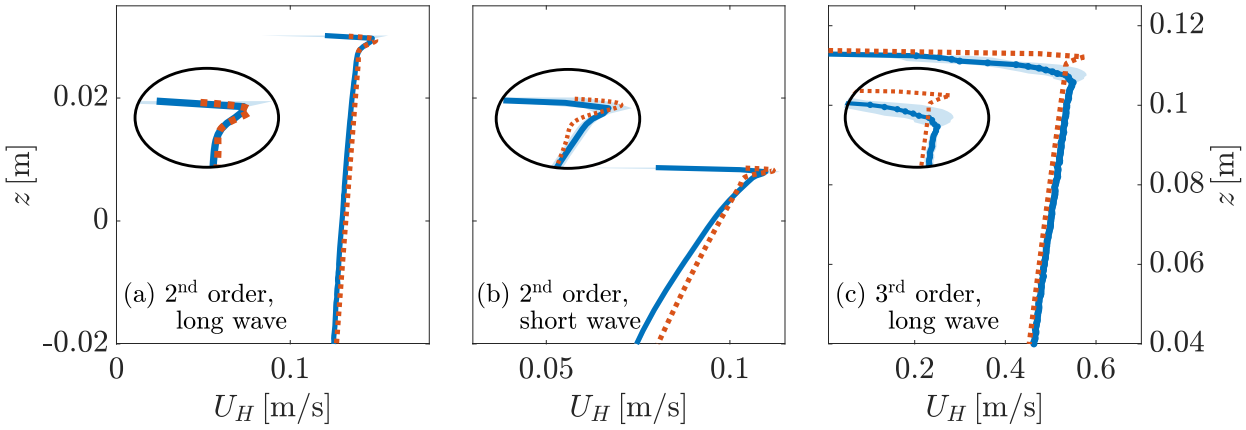

Fig. 14. Crest-phase horizontal velocity profiles beneath the flexible structure for three representative regimes: (a) W3-2, (b) W6-2, and (c) W3-3. Insets (circled) show the near-interface boundary-layer region; shaded bands indicate the 95% confidence interval of wave-to-wave variability within each run.

CRediT authorship contribution statement

Esra Uksul: Writing – original draft, Visualization, Formal analysis, Data curation; **Angeliki Laskari:** Writing – review & editing, Supervision, Conceptualization; **Sebastian Schreier:** Writing – review & editing, Supervision, Project administration; **Christian Poelma:** Writing – review & editing, Supervision, Funding acquisition, Conceptualization.

Data availability

Data will be made available on request.

Declaration of competing interest

The authors declare that they have no known competing financial interests or personal relationships that could have appeared to influence the work reported in this paper.

Appendix A. Repeatability of velocity profiles

Results in the main text were obtained from phase-averaged velocity fields based on repeated wave realizations within a single experimental run. To quantify the variability relevant to these averages and to document repeatability across independent repetitions, this appendix provides uncertainty bounds for two representative cases: W3-2 and W6-2 (Figs. A.1–A.2).

First, within-run wave-to-wave variability was evaluated from $N = 30$ repeated wave realizations at fixed phase within one run (Fig. A.1). At each vertical location, the 95% confidence interval (CI) of the mean profile was estimated as $\Delta U_{95}(z) = t_{0.975,N-1}\,\sigma(z)/\sqrt{N}$, where $\sigma(z)$ is the sample standard deviation across realizations and $t_{0.975,N-1}$ is the Student-t multiplier.

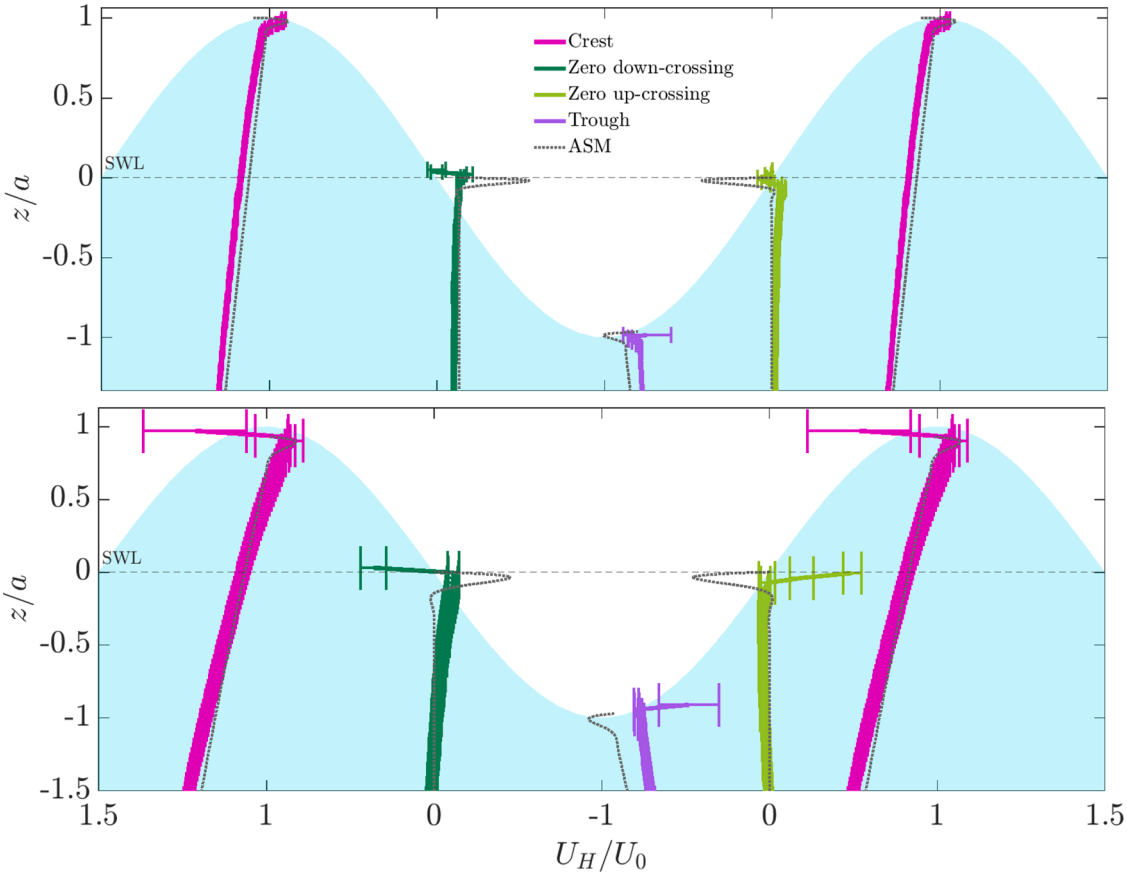

Fig. A.1. Normalized horizontal velocity profiles U_H/U_0 for wave case W3-2 (top) and W6-2 (bottom) at selected phases (crest, trough, and zero-crossings). Horizontal error bars indicate the 95% confidence interval of the mean profile due to wave-to-wave variability within a single run ($N = 30$). Dotted curves show the adapted Stokes model (ASM).

Second, between-run repeatability was assessed across four independent experimental runs (Fig. A.2). For each phase, a run-averaged profile was computed, and the corresponding 95% CI of the mean across runs was obtained analogously using $N = 4$ (i.e., based on the run-to-run standard deviation and a $t_{0.975,3}$ multiplier).

In both assessments, uncertainty bounds are largest close to the fluid–structure interface, where steep velocity gradients make the extracted profiles most sensitive to small vertical offsets of the detected interface and masking. This repeatability-based quantification is particularly relevant here because the derived metrics ($\delta_{5\%}$ and $U_H^{\mathrm{BL,peak}}$) are governed by near-interface gradients and therefore amplify small realization-to-realization differences in interface position. Away from the interface, in the bulk of the flow, the profiles collapse closely and the associated bounds remain small, indicating good repeatability of the measured free-stream behaviour. The bounds are generally larger for the shorter, attenuating case W6-2 than for W3-2, consistent with its greater sensitivity to local interface fluctuations and evolving forcing along the structure. These bounds quantify variability of the phase-averaged profiles and do not constitute a full systematic uncertainty budget (e.g., calibration bias).

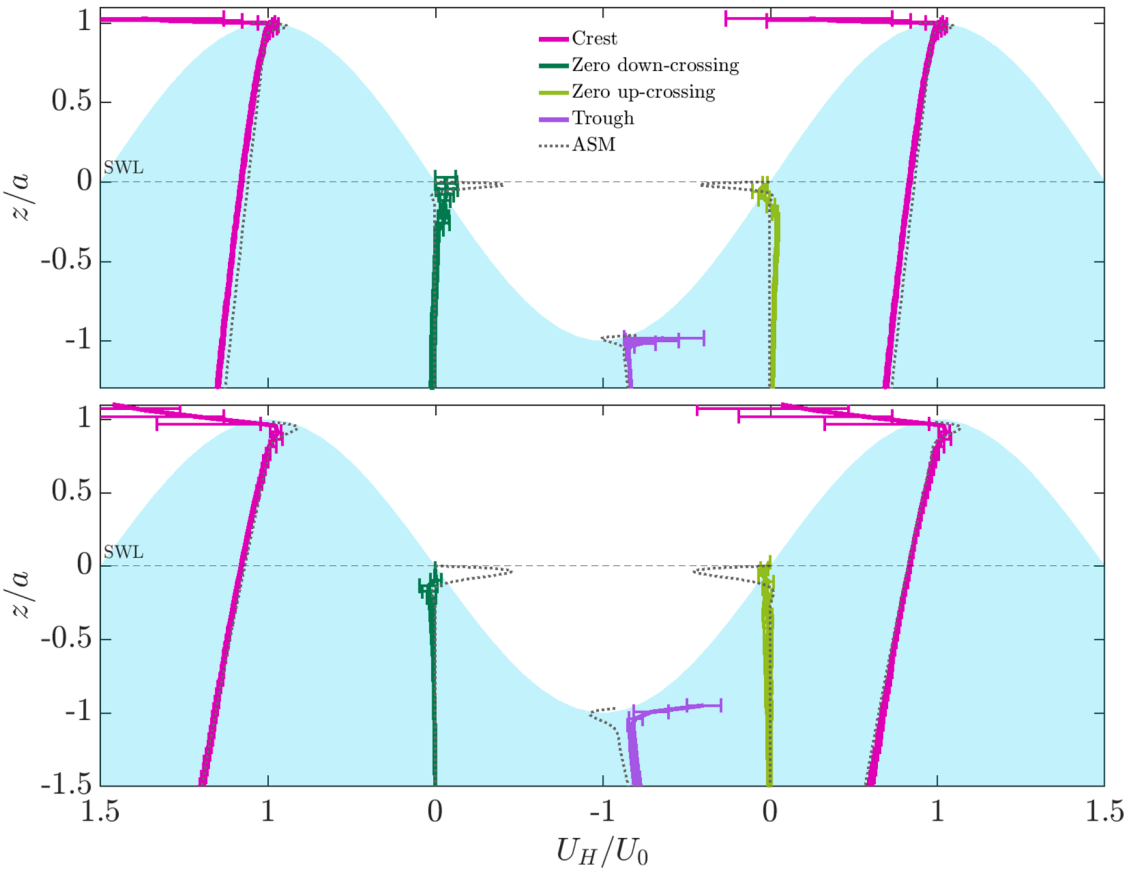

Fig. A.2. Normalized horizontal velocity profiles U_H/U_0 for wave case W3-2 (top) and W6-2 (bottom) at selected phases (crest, trough, and zero-crossings), showing repeatability across four independent runs. Horizontal error bars indicate the 95% confidence interval of the mean profile across runs ($N = 4$). Dotted curves show the adapted Stokes model (ASM).

References

Akhavan, R., Kamm, R.D., Shapiro, A.H., 1991. An investigation of transition to turbulence in bounded oscillatory stokes flows part 1. experiments. J. Fluid Mech. 225, 395–422. https://doi.org/10.1017/S0022112091002100

Berumen, J., Goree, J., 2021. Experiment and model for a stokes layer in a strongly coupled dusty plasma. Phys. Rev. E 104, 035208. https://link.aps.org/doi/10.1103/PhysRevE.104.035208

Bettencourt, J.H., Dias, F., 2018. Wall pressure and vorticity in the intermittently turbulent regime of the stokes boundary layer. J. Fluid Mech. 851, 479–506. https://doi.org/10.1017/jfm.2018.520

Coxe, D.J., Peet, Y.T., Adrian, R.J., 2022. On stokes' second problem solutions in cylindrical and cartesian domains. Phys. Fluids 34 (10). https://doi.org/10.1063/5.0118838

Coxe, D.J., Peet, Y.T., Adrian, R.J., 2024. Location and scales of drag reduction in turbulent pipe flow with wall oscillations at low reynolds number. Phys. Rev. Fluids 9, 114601. https://link.aps.org/doi/10.1103/PhysRevFluids.9.114601

Dean, R.G., 1990. Water wave kinetics: state of the art and future research needs.

Fielding, A., Ivey, G.N., Jones, A.E., 2013. Flow separation and resuspension beneath shoaling nonlinear internal waves. Cont. Shelf Res. 64, 26–36. https://doi.org/10.1029/2007JC004411

Herman, A., 2017. Wave-induced stress and breaking of sea ice in a coupled hydrodynamic discrete-element wave–ice model. Cryosphere 11 (6), 2711–2725.

Hermans, A.J., 2004. Interaction of free-surface waves with floating flexible strips. J. Eng. Math. 49 (2), 133–147. https://doi.org/10.1023/B:ENGI.0000017477.58851.af

Imberger, J., 1998. Flux paths in a stratified lake. In: Physical Processes in Lakes and Oceans. Coastal and Estuarine Studies, pp. 1–17. https://doi.org/10.1029/CE054p0001

Jabbari, A., Boegman, L., 2021. Parameterization of oscillating boundary layers in lakes and coastal oceans. Ocean Modell. 160 (February), 101780. https://doi.org/10.1016/j.ocemod.2021.101780

Jensen, B.L., Sumer, B.M., Fredsoe, J., 1989. Turbulent oscillatory boundary layers at high Reynolds numbers. J. Fluid Mech. 206, 265–297. https://doi.org/10.1017/S0022112089002302

Keane, R.D., Adrian, R.J., 1990. Optimization of particle image velocimeters. i. double pulsed systems. Meas. Sci. Technol. 1 (11), 1202. https://doi.org/10.1117/12.35018

Kearney, S., O'Hern, T., Grasser, T., Dimiduk, T., Roberts, J., Gailani, J., 2009. Turbulence structure in oscillating channel flow. In: 47th AIAA Aerospace Sciences Meeting Including the New Horizons Forum and Aerospace Exposition, p. 71.

Le Méhauté, B., 2013. An Introduction to Hydrodynamics and Water Waves. Springer Science & Business Media.

Lorke, A., Umlauf, L., Jonas, T., Wüest, A., 2002. Dynamics of turbulence in low-speed oscillating bottom-boundary layers of stratified basins. Environ. Fluid Mech. 2 (4), 291–313. https://doi.org/10.1023/A:1020450729821

Mellor, G., 2002. Oscillatory bottom boundary layers. J. Phys. Oceanogr. 32 (11), 3075–3088. https://doi.org/10.1175/1520-0485(2002)032%3C3075:OBBL%3E2.0.CO;2
Mosig, J.E.M., Montiel, F., Squire, V.A., 2015. Comparison of viscoelastic-type models for ocean wave attenuation in ice-covered seas. J. Geophys. Res. Oceans 120 (9), 6072–6090. https://doi.org/10.1002/2015JC010881
Munk, W.H., 1966. Abyssal recipes. Deep-Sea Res. Oceanograph. Abstracts 13 (4), 707–730. https://doi.org/10.1016/0011-7471(66)90602-4
National Research Council, 1994. Twenty-second symposium on naval hydrodynamics. The National Academies Press, Washington, DC. https://nap.nationalacademies.org/read/9223/chapter/7
Nielsen, P., 1992. Coastal Bottom Boundary Layers and Sediment Transport. Vol. 4. World scientific.
Orzech, M., Yu, J., Wang, D., Landry, B., Zuniga-Zamalloa, C., Braithwaite, E., Trubac, K., Gray, C., 2022. Laboratory measurements of surface wave propagation through ice floes in salt water. J. Mar. Sci. Eng. 10 (10). https://doi.org/10.3390/jmse10101483
Rabault, J., Sutherland, G., Jensen, A., Christensen, K.H., Marchenko, A., 2019. Experiments on wave propagation in grease ice: combined wave gauges and particle image velocimetry measurements. J. Fluid Mech. 864, 876–898. https://doi.org/10.1017/jfm.2019.16
Ronald, L.P., Panton, L., 2013. Incompressible flow.
Sana, A., Tanaka, H., 2007. Full-range equation for wave boundary layer thickness. Coastal Eng. 54 (8), 639–642. https://doi.org/10.1016/j.coastaleng.2007.01.011
Schlichting, H., Kestin, J., 1961. Boundary Layer Theory. Vol. 121. Springer.
Schreier, S., Jacobi, G., 2021a. Experimental investigation of wave interaction with a thin floating sheet. Int. J. Offshore Polar Eng. 31 (4), 435–444. https://doi.org/10.17736/ijope.2021.mk76
Schreier, S., Jacobi, G., 2021b. Measuring hydroelastic deformation of very flexible floating structures. In: WCFS2020: Proceedings of the Second World Conference on Floating Solutions, Rotterdam, pp. 347–371. https://doi.org/10.1007/978-981-16-2256-4
Sleath, J.F.A., 1987. Turbulent oscillatory flow over rough beds. J. Fluid Mech. 182, 369–409. https://doi.org/10.1017/S0022112089002302
Squire, V.A., 2007. Of ocean waves and sea-ice revisited. Cold Reg. Sci. Technol. 49 (2), 110–133. https://doi.org/10.1016/j.coldregions.2007.04.007
Sree, D. K.K., Law, A. W.K., Shen, H.H., 2018. An experimental study on gravity waves through a floating viscoelastic cover. Cold Reg. Sci. Technol. 155 (August), 289–299. https://doi.org/10.1016/j.coldregions.2018.08.013
Stoker, J.J., 1947. Surface waves in water of variable depth. Q. Appl. Math. 5 (1), 1–54. https://doi.org/10.1090/qam/22135
Sutherland, G., Halsne, T., Rabault, J., Jensen, A., 2017. The attenuation of monochromatic surface waves due to the presence of an inextensible cover. Wave Motion 68, 88–96. https://doi.org/10.1016/j.wavemoti.2016.09.004
Suzuki, H., Shugar, T.A., Bhattacharya, B., Riggs, H.R., Seto, H., Hudson, D.A., Fujikubo, M., Yasuzawa, Y., Shin, H., 2007. Very large floating structures. Proc. Int. Conf. Offshore Mech. Arctic Eng. - OMAE 2 (July 2014), 597–608. https://doi.org/10.1115/OMAE2007-29758
Suzuki, H., Yoshida, K., 1996. Design flow and strategy for safety of very large floating structure. In: Proceedings of Int Workshop on Very Large Floating Structures, VLFS. Vol. 96, pp. 21–27.
Uksul, E., Laskari, A., Schreier, S., Poelma, C., 2025. Velocity field measurements under very large floating structures interacting with surface waves. Ocean Eng. 315, 119759.
Wang, C.M., Tay, Z.Y., 2011. Very large floating structures: applications, research and development. Procedia Eng. 14, 62–72. https://doi.org/10.1016/j.proeng.2011.07.007
Weber, J.E., 1987. Wave attenuation and wave drift in the marginal ice zone. J. Phys. Oceanogr. 17 (12), 2351–2361. https://doi.org/10.1175/1520-0485(1987)017<2351:WAAWDI>2.0.CO;2
Westerweel, J., 1993. Digital particle image velocimetry: theory and application. PhD Thesis, Delft University of Technology. 237.
Xu, Z., Guyenne, P., 2023. Nonlinear potential flow simulations of wave propagation through ice floes. Ocean Modell. . https://doi.org/10.1016/j.ocemod.2022.102139
Yiew, L.J., Parra, S.M., Wang, D., Sree, D.K.K., Babanin, A.V., Law, A.W.K., 2019. Wave attenuation and dispersion due to floating ice covers. Appl. Ocean Res. 87 (March), 256–263. https://doi.org/10.1016/j.apor.2019.04.006
You, Z.J., Wilkinson, D.L., Nielsen, P., 1992. Velocity distribution in turbulent oscillatory boundary layer. Coastal Eng. 18 (1–2), 21–38. https://doi.org/10.1016/0378-3839(92)90003-D
Yuan, J., Madsen, O.S., 2014. Experimental study of turbulent oscillatory boundary layers in an oscillating water tunnel. Coastal Eng. 89, 63–84. https://doi.org/10.1016/j.coastaleng.2014.03.007
Zhang, G., Li, Q., Jiang, C., el Moctar, O., Sun, Z., 2025. Constraint effects on the hydroelasticity of very large floating structures. Ocean Eng. 331, 121304. https://doi.org/10.1016/j.oceaneng.2025.121304
Zhang, M., Schreier, S., 2022. Review of wave interaction with continuous flexible floating structures. Ocean Eng. 264. https://doi.org/10.1016/j.oceaneng.2022.112404
Zhao, K., Liu, P. L.F., 2022. On Stokes wave solutions. Proc. R. Soc. A: Math. Phy. Eng. Sci. 478 (2258). https://doi.org/10.1098/rspa.2021.0732
Zhao, X., Shen, H.H., 2015. Wave propagation in frazil/pancake, pancake, and fragmented ice covers. Cold Reg. Sci. Technol. 113, 71–80. https://doi.org/10.1016/j.coldregions.2015.02.007